AFRL-AFOSR-UK-TR-2019-0047

Effective First Principles Modeling of Semiconductor Lasers

Ortwin Hess
IMPERIAL COLLEGE OF SCIENCE TECHNOLOGY & MEDICINE
EXHIBITION RD
LONDON, SW7 2BT
GB

09/11/2019
Final Report

Air Force Research Laboratory
Air Force Office of Scientific Research
European Office of Aerospace Research and Development
Unit 4515 Box 14, APO AE 09421

REPORT DOCUMENTATION PAGE

Form Approved
OMB No. 0704-0188

1. REPORT DATE *(DD-MM-YYYY)*	2. REPORT TYPE	3. DATES COVERED *(From - To)*
11-09-2019	Final	01 Sep 2014 to 31 Aug 2018

4. TITLE AND SUBTITLE
Effective First Principles Modeling of Semiconductor Lasers

5a. CONTRACT NUMBER

5b. GRANT NUMBER
FA9550-14-1-0181

5c. PROGRAM ELEMENT NUMBER
61102F

6. AUTHOR(S)
Ortwin Hess

5d. PROJECT NUMBER

5e. TASK NUMBER

5f. WORK UNIT NUMBER

7. PERFORMING ORGANIZATION NAME(S) AND ADDRESS(ES)
IMPERIAL COLLEGE OF SCIENCE TECHNOLOGY & MEDICINE
EXHIBITION RD
LONDON, SW7 2BT GB

8. PERFORMING ORGANIZATION REPORT NUMBER

9. SPONSORING/MONITORING AGENCY NAME(S) AND ADDRESS(ES)
EOARD
Unit 4515
APO AE 09421-4515

10. SPONSOR/MONITOR'S ACRONYM(S)
AFRL/AFOSR IOE

11. SPONSOR/MONITOR'S REPORT NUMBER(S)
AFRL-AFOSR-UK-TR-2019-0047

12. DISTRIBUTION/AVAILABILITY STATEMENT
A DISTRIBUTION UNLIMITED: PB Public Release

13. SUPPLEMENTARY NOTES

14. ABSTRACT
Simulation developed and potentially providing to AFRL and DSTL.

15. SUBJECT TERMS
Semiconductor Lasers, maxwell bloch equations, diode pumped solid state laser physics, many body apprach to dpssl, EOARD

16. SECURITY CLASSIFICATION OF:			17. LIMITATION OF ABSTRACT	18. NUMBER OF PAGES	19a. NAME OF RESPONSIBLE PERSON
a. REPORT	b. ABSTRACT	c. THIS PAGE			LOCKWOOD, NATHANIEL
Unclassified	Unclassified	Unclassified	SAR		19b. TELEPHONE NUMBER *(Include area code)* 011-44-1895-616005

Standard Form 298 (Rev. 8/98)
Prescribed by ANSI Std. Z39.18

Effective First Principles Modeling of Semiconductor Lasers

Full-Time-Domain (FDTD) Maxwell-Bloch Modelling of Semiconductor Lasers Under Non-equilibrium Operating Conditions: From Semiconductors Quantum Wells to Monolayer Semiconductors

Stefano Guazzotti and Ortwin Hess

November 27, 2017

Contents

1 Introduction

Semiconductors exhibit a multitude of nonlinear optical responses for resonant as well as non-resonant excitation.[1] One of the most prominent nonlinear features is the generation of higher harmonics of the exciting frequency. When the frequency of the incoming field is tripled one speaks of third harmonic generation (THG). Such THG can be employed in spectroscopy and provides important insights into biological processes[2, 3] or even for palaeontology.[4] In semiconductors, THG has, for example, been studied in coupled quantum wells,[5, 6] quantum cascade structures,[7] quantum wires and dots,[8, 9] while it is also of interest in newly developed materials like graphene[10] and atomically thin semiconductors.[11]

In order to understand THG one requires a description of the optical fields and the material which is excited by them and generates the nonlinear interaction. Here we focus on the photointeraction of semiconductor quantum wells (QW) with ultrashort light pulses. To this end, we employ an auxiliary differential equation finite difference time domain (FDTD) approach to describe the dynamics of the light field along with the dynamics of the carriers in the QW. This approach goes beyond rotating wave approximation and slowly-varying envelope approximation, allowing to treat fundamental and third harmonic on the same footing and describe photonic structures that vary on scales much smaller than the wavelength. The combination of FDTD with density matrix models through auxiliary differential equations includes not only the effect of the field on the material but also self-consistently describes

the effect of the material on the field. This feature allows, for example, to describe propagation of SIT solitons in 1 and 2 dimensions[12–14] and to study loss compensation and lasing dynamics in metamaterials[15–18] or plasmonic stopped-light lasers.[19] However, the few-level models employed in those studies can not describe the complicated behavior of an interacting electron gas excited in semiconductor QWs.[20–22]

On the other hand more complex wave-vector resolved semiconductor models have been developed that also consider Coulomb interaction between excited carriers within different levels of approximation[1, 22, 23] or spatially resolved quantum kinetics calculations.[24–26] Such models have been used to investigate various non linear effects such as the two-band Mollow triplet in thin GaAs films,[27] the carrier-wave Rabi flopping in bulk GaAs[28] and THG from carbon nanotubes both in the perturbative and non-perturbative regime.[29, 30] These approaches, however, do not include the self-consistent, spatially resolved resolution of electromagnetic fields.

Combining a spatially dependent full time-domain (FDTD) approach with a description of semiconductor QWs containing a wave-vector resolved, many-level density matrix description of the QW in a two-band approximation, has been pioneered in Böhringer and Hess [31, 32] to describe the spatio-temporal dynamics of semiconductor lasers and recently to describe lasing of semiconductor nanowires.[33]

In this report we show how the model can be simplified and adapted to the simulation of spatially extended semiconductor systems, such as QW lasers. In particular, we can explore these systems beyond the previously used slowly-varying envelope approximation and therefore we are not restricted to consider a finite set of previously decided modes but all possible frequency are included in our calculation. Furthermore, both the field and the semiconductor in our model are resolved on a sub-wavelength spatial scale, allowing us to access previously inaccessible dynamics. What we are now concentrating on is exploring how the appearance of wavelength sized structures in the carrier density affects the behaviour of the semiconductor laser.

Our recently published work in which the model described here is used and extended to include Coulomb interaction in Hartree-Fock approximation, allows us to describe the excitonic nature of the QW absorption[34]. The model is used to explore the response to a ultrashort pulse excitation of a QW embedded in a Bragg mirror structure typical for a semiconductor saturable absorber mirror (SESAM). We observed the carrier dynamics associated with excitation of the QW exciton and study the intensity dependence of THG generated from this QW. We find that the power-law exponent of the intensity dependence of the THG strongly varies with excitation frequency. For far off-resonant pulses the expected cubic behavior is found, while for pulses resonant with the exciton energy the exponent is reduced due to saturation effects. Similar findings have been reported in theoretical and experimental studies on the excitation of carbon nanotubes with ultrashort laser pulses.[29, 30]

2 Theoretical model

We describe the quantum well (QW) as a (quasi) two-dimensional infinitely extended system, resulting in a two-dimensional reciprocal space $\mathbf{k} = (k_x, k_y)$. Since we are interested in the interrelationship of carriers and light dynamics, we are only interested in the region of the semiconductor band structure which lies in the proximity of the (direct) band-gap. We therefore apply a parabolic-band/effective-mass approximation to the lowermost conduction and uppermost valence bands which are respectively characterised by the effective electron, m_e, and hole, m_h, masses. At the same time the electron movement in the cross direction is confined by the difference in band structure between the well material and the barrier material, resulting in a discrete spectrum of subbands.

2.1 Envelope function approximation (EFA)

In order to calculate the discrete spectrum of subbands we apply the envelope function approximation and consider the movement in the cross direction as an independent one-dimensional quantum system subject to a potential well whose depth is determined by the bandgap mismatch between well and barriers material.

The difference in bandgap

$$\Delta_g = \varepsilon_g^b - \varepsilon_g^w \tag{1}$$

has to be split between electrons and holes. To do so we consider that at equilibrium there should be no exchange of carriers between well and barriers, i.e., the two materials should have the same chemical potential $\mu^b = \mu^w$. By assuming both to be intrinsic (i.e., undoped and with μ well within the bandgap) and at equilibrium (i.e., no inversion) we can express the chemical potential as

$$\mu^\nu = \frac{1}{2}\varepsilon_g^\nu + \frac{3}{4}k_B T \ln\left(\frac{m_e^\nu}{m_h^\nu}\right) \qquad \nu = b, w \tag{2}$$

where the zero of energy is set at the top of the respective valence band. By setting a common reference for the energy at the top of the valence band in the barrier region, we get

$$\mu^b = \frac{1}{2}\varepsilon_g^b + \frac{3}{4}k_B T \ln\left(\frac{m_e^b}{m_h^b}\right) \tag{3a}$$

$$\mu^w = \frac{1}{2}\varepsilon_g^w + \frac{3}{4}k_B T \ln\left(\frac{m_e^w}{m_h^w}\right) + V_h, \tag{3b}$$

which, together with $V_e + V_h = \varepsilon_g^b - \varepsilon_g^w$, can be solved for the confining potential for electrons and holes, giving

$$V_e = \frac{1}{2}\Delta_g + \frac{3}{4}k_B T \ln\left(\frac{m_h^w}{m_h^b}\frac{m_e^b}{m_e^w}\right) \tag{4a}$$

$$V_h = \frac{1}{2}\Delta_g + \frac{3}{4}k_B T \ln\left(\frac{m_h^b}{m_h^w}\frac{m_e^w}{m_e^b}\right). \tag{4b}$$

This fully defines the piecewise Hamiltonian of the system as that of a particle subject to the potential well shown in Fig. 1a:

$$\mathcal{H}_{e/h} = \begin{cases} -\frac{\hbar^2}{2m_{e/h}^b}\frac{\partial^2}{\partial z^2} + V_{e/h} & \text{for } z \le -\frac{L}{2} \\ -\frac{\hbar^2}{2m_{e/h}^w}\frac{\partial^2}{\partial z^2} & \text{for } -\frac{L}{2} \le z \le \frac{L}{2} \\ -\frac{\hbar^2}{2m_{e/h}^b}\frac{\partial^2}{\partial z^2} + V_{e/h} & \text{for } z \ge \frac{L}{2} \end{cases} \tag{5}$$

which can be solved similarly to the common quantum mechanical problem of a particle in a finite depth potential well, the only difference being the presence of different masses in different regions, resulting in a modified boundary condition for the derivative of the wave function at $z = \pm\frac{L}{2}$;

$$\left.\frac{1}{m_{e/h}^w}\partial_z\psi_{e/h}(z)\right|_{\frac{L}{2}^-} = \left.\frac{1}{m_{e/h}^b}\partial_z\psi_{e/h}(z)\right|_{\frac{L}{2}^+} \tag{6}$$

As a result of the EFA, the total energy of an electron/hole with respect to the bottom of the respective bulk band is

$$\varepsilon_{e/h}^n(\mathbf{k}) = \frac{\hbar^2 k^2}{2m_{e/h}} + \epsilon_{e/h}^n, \tag{7}$$

with the two-dimensional wave-vector, $\mathbf{k}$, and the discrete index $n = 1, 2, \ldots n_{max}$, see Fig. 1b. The dipole matrix element for the transition from the j-th hole subband to the $i-$th electron subband is obtained from the 1D envelope functions as

$$d_{i,j} = d_{cv}\int \mathrm{d}z\psi_{h,j}^*(z)\,\psi_{e,i}(z), \tag{8}$$

where d_{cv} is the dipole matrix element of the $v \to c$ transition in the bulk material. As a consequence optical transitions are only allowed between subbands with the same inversion parity, and the dominant transitions will be $i \to i$.

From here on we consider a single subband model, where we only consider the $i = 1$ subband for electrons and holes and therefore drop from the notation all indeces referring to subbands.

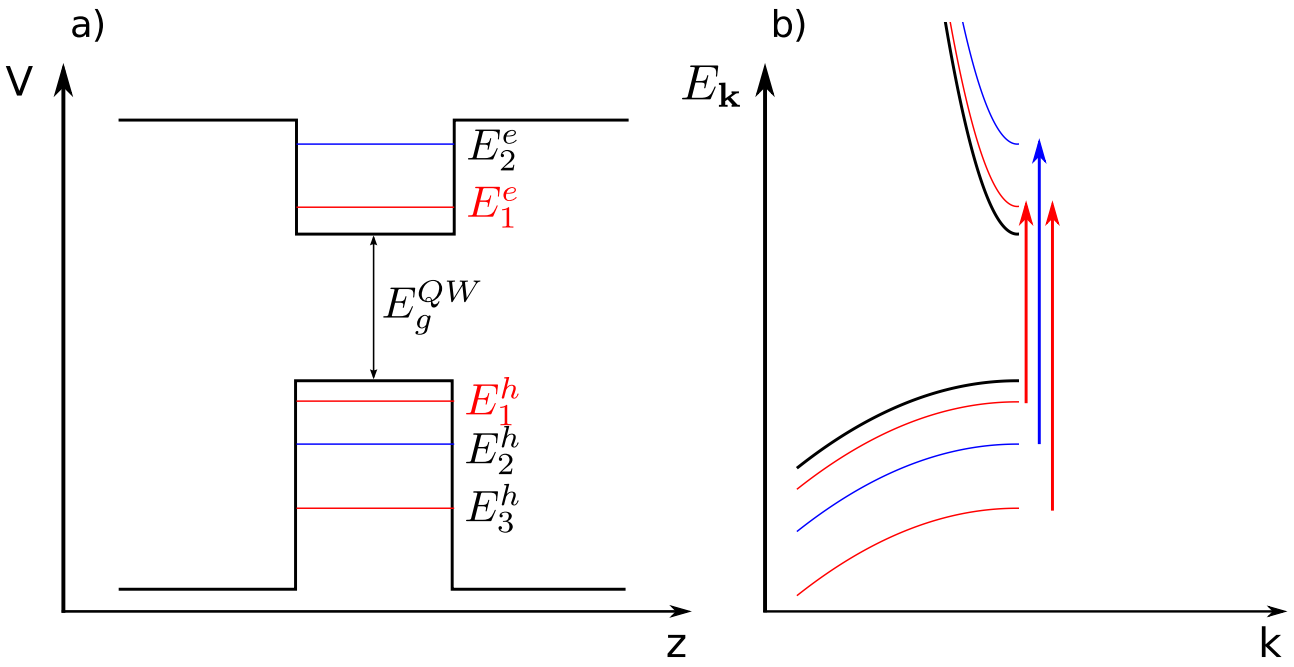

Figure 1: (a) Bandgap energy in the cross direction of the QW, showing the confining potentials of electrons and holes as well as the eigenvalues obtained by solving the Hamiltonian in eq. 5. (b) QW energy subbands (eq. 7)

		$\varepsilon_g^{b/w}(eV)$	$m_e(m)$	$m_h(m)$	$\epsilon_e^1(meV)$	$\epsilon_h^1(meV)$	$d_{1,1}/d_{cv}$
barrier	$Al_{0.3}Ga_{0.7}As$	1.798	0.0879	0.585	34.4	5.9	0.9848
QW	GaAs	1.424	0.063	0.51			

2.2 Time domain response of QW

By neglecting Coulomb interaction, the QW band structure can be described as a set of non-interacting two-level system, whose transition frequency is a function of the wave-vector $\mathbf{k}$. We can therefore write the Bloch equations for each state as

$$\partial_t \mathcal{P}_{\mathbf{k}}(\mathbf{r},t) = -(\mathrm{i}\omega_{\mathbf{k}} + \gamma)\,\mathcal{P}_{\mathbf{k}}(\mathbf{r},t) - \mathrm{i}\frac{e\mathbf{d}\cdot\mathbf{E}(\mathbf{r},t)}{\hbar}\left(f_{\mathbf{k}}^e + f_{\mathbf{k}}^h - 1\right) \tag{9a}$$

$$\partial_t n_{\mathbf{k}}^{e/h} = \mathrm{i}\frac{e\mathbf{d}\cdot\mathbf{E}(\mathbf{r},r)}{\hbar}\left(\mathcal{P}_{\mathbf{k}}^* - \mathcal{P}_{\mathbf{k}}\right) = 2\frac{e\mathbf{d}\cdot\mathbf{E}}{\hbar}\Im\left(\mathcal{P}_{\mathbf{k}}\right), \tag{9b}$$

with the complex polarisation, $\mathcal{P}_{\mathbf{k}} = p_{\mathbf{k}} + p'_{\mathbf{k}}$, the transition frequency, $\omega_{\mathbf{k}} = \left(\varepsilon_e(\mathbf{k}) + \varepsilon_h(\mathbf{k}) + \varepsilon_g\right)/\hbar$ (see eq. 7), the polarisation dephasing, γ, the dipole matrix element, $\mathbf{d}$ (see eq. 8), the time- and space-resolved electric field, $\mathbf{E}$, and the equilibrium Fermi-Dirac distribution for electrons and holes in effective mass approximation, $f_{\mathbf{k}}^e$ and $f_{\mathbf{k}}^h$, which depend on position and time through their dependence on the chemical potential. Furthermore, we only track the change in density at the macroscopic level, $\partial_t N$, i.e., by performing a $\mathbf{k}$-sum of eq. 9b. We can split eq. 9a in its real ($p_{\mathbf{k}}$) and imaginary ($p'_{\mathbf{k}}$) parts

$$\partial_t p_{\mathbf{k}}(\mathbf{r},t) = \omega_{\mathbf{k}} p'_{\mathbf{k}}(\mathbf{r},t) - \gamma p_{\mathbf{k}}(\mathbf{r},t) \tag{10a}$$

$$\partial_t p'_{\mathbf{k}}(\mathbf{r},t) = -\omega_{\mathbf{k}} p_{\mathbf{k}}(\mathbf{r},t) - \gamma p'_{\mathbf{k}}(\mathbf{r},t) - \frac{e\mathbf{d}\cdot\mathbf{E}(\mathbf{r},t)}{\hbar}\left(f_{\mathbf{k}}^e + f_{\mathbf{k}}^h - 1\right) \tag{10b}$$

and eliminate $p'_{\mathbf{k}}$ to get a second order differential equation in the real part of the polarisation

$$\left(\partial_t^2 + 2\gamma\partial_t + \left(\omega_{\mathbf{k}}^2 + \gamma^2\right)\right) p_{\mathbf{k}}(\mathbf{r},t) = \frac{e\omega_{\mathbf{k}}\mathbf{d}\cdot\mathbf{E}(\mathbf{r},t)}{\hbar}\left(1 - f_{\mathbf{k}}^e(\mathbf{r},t) - f_{\mathbf{k}}^h(\mathbf{r},t)\right). \tag{11}$$

From this, we can calculate the (2D) macroscopic polarisation as

$$\mathbf{P}_2(\mathbf{r},t) = \frac{2e\mathbf{d}}{A}\sum_{\mathbf{k}} p_{\mathbf{k}}(\mathbf{r},t) \tag{12}$$

and finally get the "proper" macroscopic polarisation, which will enter Maxwell's equations, as

$$\mathbf{P}(\mathbf{r},t) = \frac{N_{QW}}{L_{act}}\mathbf{P}_2(\mathbf{r},t) \tag{13}$$

where N_{QW} is the number of QWs in the active region of length L_{act}.

The two-dimensional sheet-density of carriers as a spatio-temporal quantity is tracked at the macroscopic level

$$\partial_t N(\mathbf{r},t) = \frac{1}{A}\sum_{\mathbf{k}} \partial_t n^e_{\mathbf{k}}(\mathbf{r},t) - \gamma_{nr} N(\mathbf{r},t) \tag{14}$$

where γ_{nr} is the non radiative decay rate and $\sum_{\mathbf{k}} \partial_t n^e_{\mathbf{k}}(\mathbf{r},t)$ is obtained from eq. 9b. By exploiting eq. 10a, rewritten as

$$p'_{\mathbf{k}}(\mathbf{r},t) = \frac{1}{\omega_{\mathbf{k}}}\left(\partial_t p_{\mathbf{k}}(\mathbf{r},t) + \gamma p_{\mathbf{k}}(\mathbf{r},t)\right), \tag{15}$$

we can write eq. 14 as

$$\partial_t N(\mathbf{r},t) = \frac{1}{A}\mathbf{E}(\mathbf{r},t)\cdot(\partial_t \mathbf{Q} + \gamma \mathbf{Q}) - \gamma_{nr} N, \tag{16}$$

where $\mathbf{Q}$ is

$$\mathbf{Q} = \frac{2e\mathbf{d}}{A}\sum_{\mathbf{k}} \frac{p_{\mathbf{k}}}{\hbar\omega_{\mathbf{k}}}. \tag{17}$$

The microscopic occupations entering eq. 11 are calculated as

$$f^{e/h}_{\mathbf{k}}\left(\mu^{e/h}\right) = \frac{1}{\mathrm{e}^{\beta\left(\varepsilon^{e/h}_{\mathbf{k}} - \mu^{e/h}\right)} + 1} \tag{18}$$

with $\mu^{e/h}$ the quasi-chemical potential for electrons (holes) obtained from the macroscopic density through

$$\beta\mu^{e/h}(N) = \ln\left(\mathrm{e}^{\hbar^2\beta\pi N/m_{e/h}} - 1\right). \tag{19}$$

The model for the QW is now complete and its main equations are 11 and 16 with the auxiliary equations 17, 18 and 19 and the coupling to the field provided through equation 13.

2.3 Gain model and further simplifications

The system we are simulating is one dimensional, therefore $\mathbf{r} \to x$. Furthermore we can focus on a single light polarisation so that we don't need to consider the electric field as a vector, resulting in $\mathbf{E} \to E$ and $\mathbf{d} \to d$.

If we now look at eq. 11 and recall that we have an isotropic energy dispersion $\varepsilon_{e/h}(\mathbf{k}) = \varepsilon_{e/h}(k)$ we can conclude that in our model the microscopic polarisation will always be isotropic. We can therefore replace everywhere the index $\mathbf{k}$ with its magnitude $k = |\mathbf{k}|$ and introduce the density of states for a two dimensional system

$$D(k)\,\mathrm{d}k = \frac{k}{\pi}\mathrm{d}k. \tag{20}$$

Lastly we discretize the energy bands in such a way as to get a set of states equally spaced in transition frequency. This means that the set of two level systems we will use to describe the semiconductor is linear in transition frequency ω:

$$\varepsilon_e(\omega) = \frac{m^*}{m_e}(\hbar\omega - \varepsilon_g) \tag{21a}$$

$$\varepsilon_h(\omega) = \frac{m^*}{m_h}(\hbar\omega - \varepsilon_g) \tag{21b}$$

$$k = \frac{\sqrt{2m^*(\hbar\omega - \varepsilon_g)}}{\hbar} \tag{21c}$$

where m^* is the elctron-hole reduced mass and we are now setting $\varepsilon_{e/h}(\omega)$ with respect to the subband and including the subband energy in the gap, i.e., $\varepsilon_g = \varepsilon_g + \epsilon_e + \epsilon_h$. This also results in the new density of states

$$D(\omega)\,\mathrm{d}k = \frac{m^*}{\pi\hbar}\mathrm{d}\omega, \tag{22}$$

allowing us to transform all the k-sums of the model into integrals in energy space

$$P(x,t) = \frac{N_{QW}}{L_{act}}\frac{m^*}{\pi\hbar}\int_{\omega_g}^{\omega_{max}} q(\omega)\,\mathrm{d}\omega \tag{23a}$$

$$Q(x,t) = \frac{m^*}{\pi\hbar}\int_{\omega_g}^{\omega_{max}} \frac{q(\omega)}{\hbar\omega}\mathrm{d}\omega \tag{23b}$$

where $\hbar\omega_g = \varepsilon_g$ is the frequency corresponding to the band gap and ω_{max} is the maximum frequency included in the model and $q(\omega) = 2ed\,p(k(\omega))$.

2.4 Diffusion and pumping

Following Hess and Kuhn [35], we add spatial transport of carriers through means of a macroscopic diffusion equation in the density

$$\partial_t N(x,t) = D\partial_x^2 N(x,t). \tag{24}$$

Pumping of carrier is assumed to be from applying a constant current density through the active region. By further assuming that the injected carriers reach the active region following an equilibrium distribution[36], we can formulate pumping macroscopically as

$$\partial_t N(x,t) = \frac{\eta J}{e}, \tag{25}$$

where η is the injection efficiency and J the applied current density.

As a result of all these added terms, the density in the model evolves according to

$$\partial_t N(x,t) = D\partial_x^2 N(x,t) + E(x,t)\left(\partial_t Q(x,t) + \gamma Q(x,t)\right) - \gamma_{nr} N(x,t) + \frac{\eta J}{e}. \tag{26}$$

3 Results

In this section we will show some of the preliminary results obtained from the presented model with particular interest for lasing and the field dynamics and how the carrier dynamics affects the output of the laser. The simulated system is a one dimensional cut of a QW laser, where the single axis is located in the QW plane (Fig. 2). The laser is a semiconductor segment of length L described as the superposition of a background dielectric constant of $\varepsilon = 12.25$ and an active medium as described in Section 2 surrounded by air. The simulation domain is terminated through absorbing boundary conditions, in order to describe an open system, and the field propagating right is recorded before leaving through the right edge. Since the description of the field provided by the FDTD method is completely classical, one cannot rely on quantum fluctuations in the field to start the lasing process but a different mean of creating polarisation in the QW is required. This is obtained here through a "starter" field, i.e., a single pulse injected in the simulation domain through the TFSF technique and pointing at the semiconductor. The pulse is much weaker than the lasing field obtained as output and is composed of a Gaussian ramp up, followed by a sinusoidal wave and a final Gaussian ramp down.

3.1 Linear response of the QW model

We performed some initial testing of the model by looking at its response to a weak field. In this context both the pumping and diffusion effects (Eqs. 24 and 25) are turned off and the "starter" field is replaced by a very short Gaussian pulse, allowing us to look at the response over a wide spectral range.

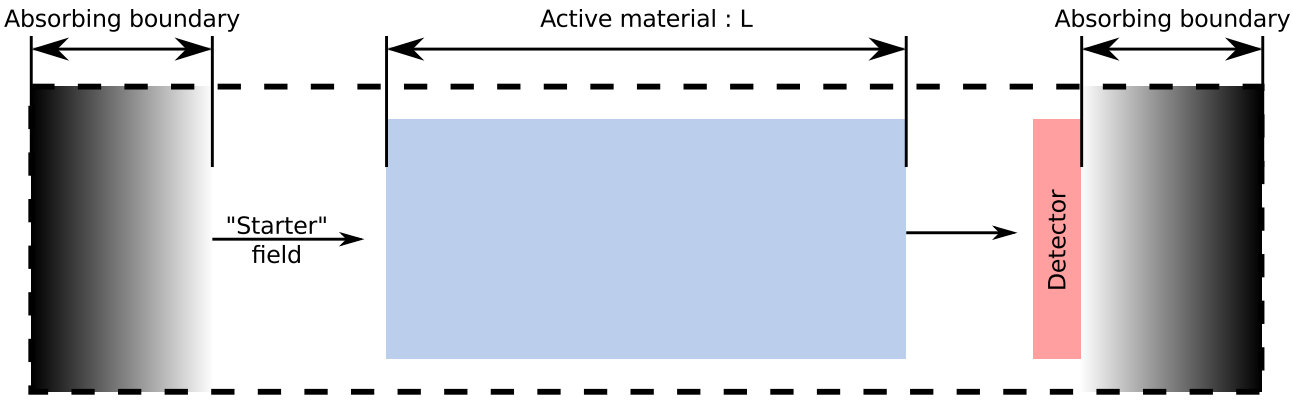

Figure 2: Graphical representation of the simulated system. The main element is a region of semiconductor (active material) of length L, described as a background dielectric constant with the addition of the QW model. The semiconductor is surrounded by air and the simulation region is delimited with absorbing boundary conditions, thus describing an open system. An initial field outside of the semiconductor is initially used to create some polarisation and the field is collected at the opposite end of the simulation domain.

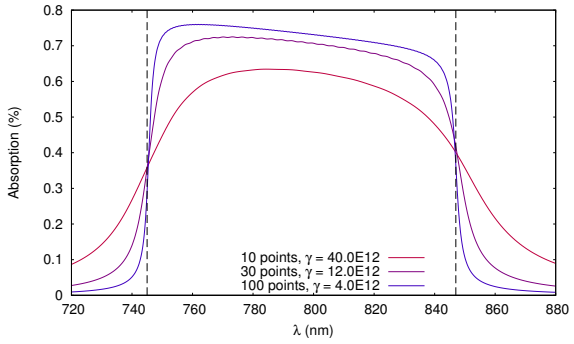

(a) Linear response of the QW model in the absorptive regime and its dependence on the number of points used to represent the electron and hole bands of the semiconductor.

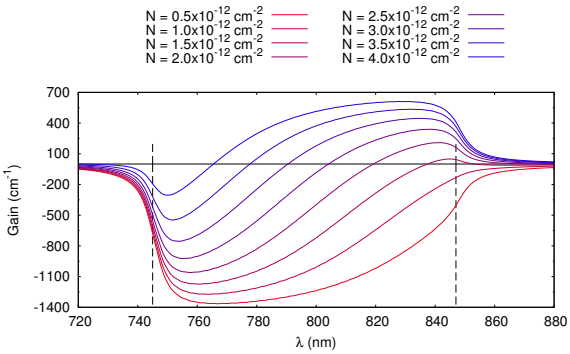

(b) Linear response of the QW model in the inverted regime for $n_k = 30$ points. Different curves correspond to different values of the density.

Figure 3: Linear response of the QW model in the absorptive and inverted regimes. The black vertical dashed lines represent the first and last point used in the model. This corresponds to the bandgap at the low energy side of the spectrum and is a suitably chosen value at the high energy one.

We initially validated the model by looking at the spectrum of the absorption from a semiconductor of $L = 20$ nm, which correspond to a single cell in the FDTD grid. The percentage of absorbed field is calculated as

$$\alpha(\omega) = 1 - \frac{E_t^2(\omega) + E_r^2(\omega)}{E_i^2(\omega)}, \tag{27}$$

where $E_i(\omega)$ is the spectrum of the incident field, $E_t(\omega)$ the spectrum of the transmitted field and $E_r(\omega)$ the one of the reflected field. Figure 3a shows that the absorption is about constant in the spectral region close to the band gap, as one would expect from looking at the joint density of states.

By looking at the linear response we can also understand how the parameters that enter the model affect the results. Figure 3a, for example, shows how the absorption depends on the number of reciprocal space points that we use to describe the system (n_k), i.e., the number of points for which Eq. 11 is solved and the integrals of Eqs. 23 are calculated over. A higher number of points will better represent the continuous k-space parametrising the semiconductor bands, whereas a smaller number will allow for a larger spatial extension of the material in the simulation.

Another important parameter to determine is the maximum energy included in the model, i.e., the upper limit of the integrals contained in Eq. 23. This has a very straightforward effect on the spectral range that we are interested in exploring, as any field beyond ω_{max} will mainly experience the background dielectric constants. It also has a more subtle relationship with the values of the macroscopic density that can be reached in the simulation. In particular as the density grows the quasi-chemical potential grows with it and it can approach ω_{max} resulting in very high occupation of most of the states included in the model. This results in a grow of the spectral region where gain is obtained at the expense of the absorptive region. This is represented in Fig. 3b, where the gain spectrum of a $L = 100$ nm region of semiconductor is shown for different values of the macroscopic sheet density, N.

3.2 Lasing

After validating the model, we explored the lasing regime in a much larger, $L = 20$ μm, semiconductor system by turning on the pumping, Eq. 25, and setting $J = 5$ A/mm^2. This allows the system to build up inversion that can act as optical gain for the field through the process of stimulated emission. As a result a field much stronger than what is used to start the process is outputted from the system, as can be seen in Fig. 4a. This is obtained in the limiting case of $D = 0$, i.e., without any form of spatial transport of carriers acting in the model. The resulting effect is that every one of the active modes impresses its own spatial profile on the density, resulting in a very strong spatial hole burning, as shown in Fig. 4c. This is the main source of the multimode behaviour that we observe in the system and that is highlighted by looking at the optical region of the spectrum, Fig. 4b. In particular, due to the absence of carrier redistribution mechanisms, the pattern burnt into the density by a mode is going to deplete the gain available to the mode itself more than that available to neighbouring modes.

Since the multimode behaviour of the system is a direct consequence of the strong spatial hole burning produced in the absence of carrier redistribution, we expect it to change when diffusion is included. This is shown in Fig. 5a, where the optical spectrum of the output field is plotted for different values of the diffusion coefficient, D. The values have been selected to be distributed over the range in which a change from multimode to singlemode behaviour is observed in our results. As expected, the stronger the diffusion is, the quicker the carriers are in redistributing themselves into a spatially homogeneous system, which naturally favours the mode located the closest to the gain maximum, cf. Fig. 3b.

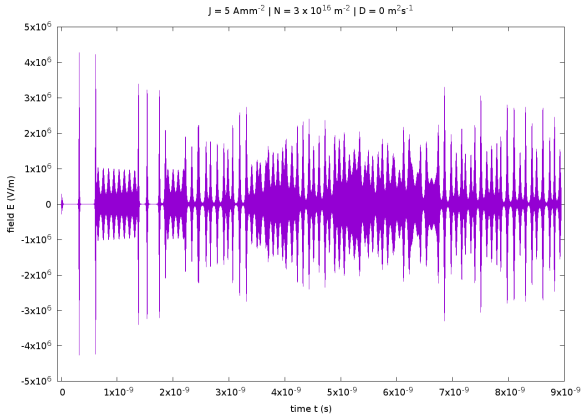

(a) Time trace of the field as recorded at the rightmost edge of the simulation domain.

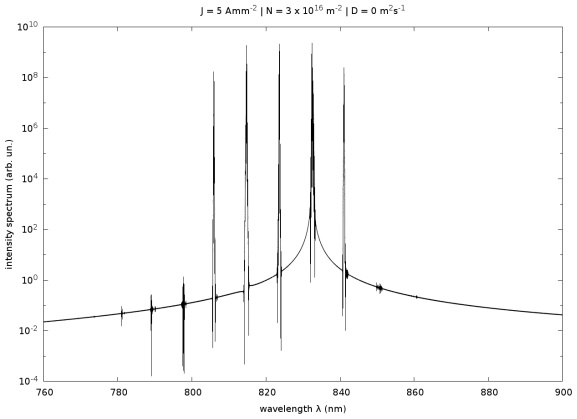

(b) Optical region of the field spectrum in Fig. 4a

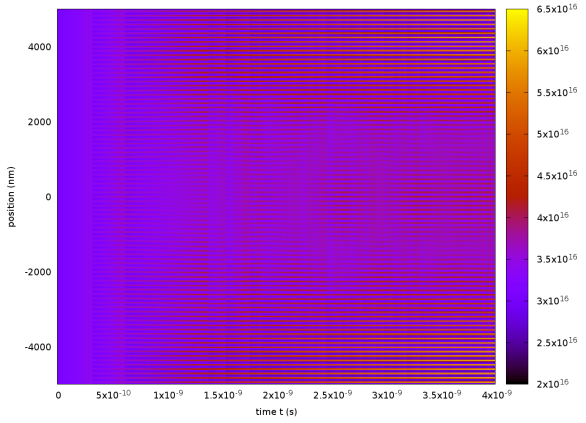

(c) Macroscopic density $N(x,t)$ as a function of space and time.

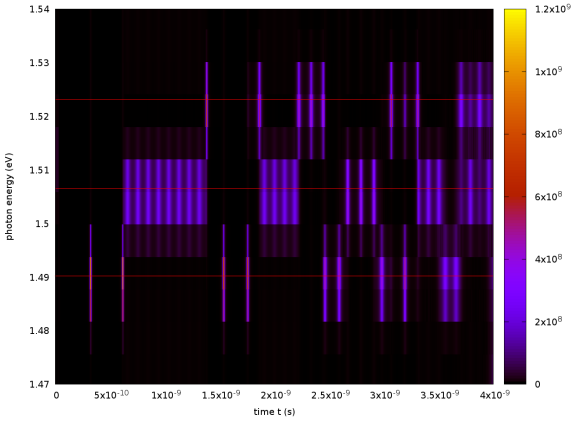

(d) Spectrogram of the output field.

Figure 4: Output field of the semiconductor laser in the case of no diffusion, i.e., $D = 0$ m^2/s.

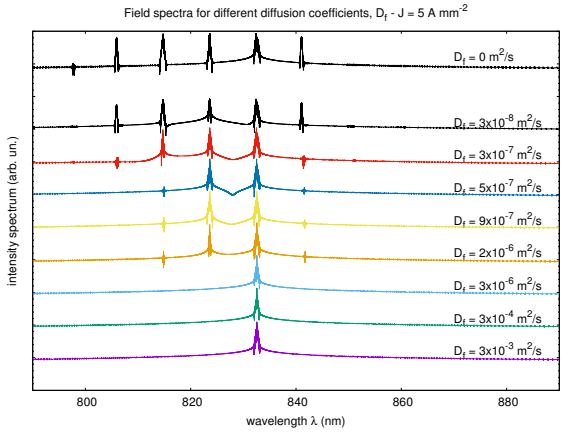

(a) Optical spectra of the output of the QW laser for different values of the diffusion coefficient. Larger values are on the bottom, while the topmost line corresponds to no diffusion.

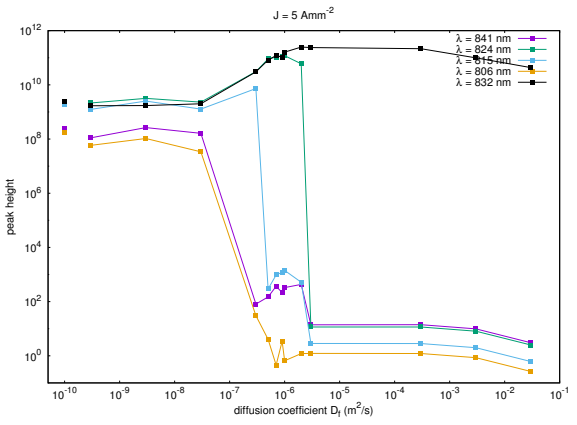

(b) Intensity of the peaks from Fig. 5a as a function of diffusion coefficient, D.

4 Linear and nonlinear optical response of semiconductor (MoS_2) monolayers

In this section we will show how the semiconductor model we developed can be easily extended in order to describe different systems. In particular, we will be focussing on monolayer transition metal dichalcogenides (TMDCs), the calculation of their optical response under weak and strong excitation. We will further show that our model is well suited to the calculation of systems consisting of emitters (i.e., TMDCs) embedded in a dielectric cavity, thus allowing the design of a dielectric or metallic environment [37] that can tailor the optical response of a suitable emitter.

This system presents few significant differences with respect to what was presented in Sec. 3, namely:

1. The semiconductor component of the system is not pumped to an inverted state, but starts at equilibrium and is electrically isolated from its environment;
2. The time scale of the dynamics is much shorter;
3. The characteristics of the semiconductor are different, especially regarding the number of involved bands and the selection rules shown for the optical transitions.

From the first two points we can also draw the conclusion that transport does not play an important role in the system dynamics.

4.1 Model

In order to adapt the model presented in Sec. 2 to the new system, we first have to take a step back and modify Eq. 9 as:

$$\partial_t \mathcal{P}_{\mathbf{k}}(\mathbf{r},t) = -(\mathrm{i}\omega_{\mathbf{k}}+\gamma)\,\mathcal{P}_{\mathbf{k}}(\mathbf{r},t) - \mathrm{i}\frac{e\mathbf{d}\cdot\mathbf{E}(\mathbf{r},t)}{\hbar}\left(n^e_{\mathbf{k}}(\mathbf{r},t)+n^h_{\mathbf{k}}(\mathbf{r},t)-1\right) \tag{28a}$$

$$\partial_t n^{e/h}_{\mathbf{k}}(\mathbf{r},t) = \mathrm{i}\frac{e\mathbf{d}\cdot\mathbf{E}(\mathbf{r},r)}{\hbar}\left(\mathcal{P}^*_{\mathbf{k}}(\mathbf{r},t)-\mathcal{P}_{\mathbf{k}}(\mathbf{r},t)\right) = 2\frac{e\mathbf{d}\cdot\mathbf{E}}{\hbar}\Im\left(\mathcal{P}_{\mathbf{k}}(\mathbf{r},t)\right), \tag{28b}$$

where we replaced the quasi-equilibrium carrier distributions $f^{e/h}_{\mathbf{k}}$ with the dynamically calculated occupations $n^{e/h}_{\mathbf{k}}(\mathbf{r},t)$. This is necessary as a consequence of the shorter time scale over which the system evolves, which breaks the quasi-equilibrium approximation employed in Eq. 9 (cf. Eq. 18) and therefore requires a model describing the microscopic dynamics of the carrier occupations as opposed to the macroscopic sheet-density of carriers.[1]

Another important difference in the system comes from considering a semiconductor in the intrinsic regime as opposed to an inverted one. As a consequence the carrier dynamics is more strongly influenced by carrier carrier interaction, leading to the necessity to include Coulomb interaction in the model. This is achieved at the Hartree-Fock level by renormalising the transition frequencies, $\widetilde{\omega}_{\mathbf{k}}(\mathbf{r},t)$, as well as introducing a renormalised Rabi frequency, $\widetilde{\Omega}_{\mathbf{k}}(\mathbf{r},t)$[34],

$$\hbar\widetilde{\omega}_{\mathbf{k}}(\mathbf{r},t) = \hbar\omega_{\mathbf{k}} - \sum_{\mathbf{k}'\neq\mathbf{k}}\left(V^{ee}_{|\mathbf{k}-\mathbf{k}'|}n^e_{\mathbf{k}'}(\mathbf{r},t) + V^{hh}_{|\mathbf{k}-\mathbf{k}'|}n^h_{\mathbf{k}'}(\mathbf{r},t)\right) \tag{29a}$$

$$\hbar\Omega_{\mathbf{k}}(\mathbf{r},t) = e\mathbf{d}\cdot\mathbf{E}(\mathbf{r},t) + \sum_{\mathbf{k}'\neq\mathbf{k}} V^{eh}_{|\mathbf{k}-\mathbf{k}'|}\mathcal{P}_{\mathbf{k}'}(\mathbf{r},t), \tag{29b}$$

where V^{ee} (V^{hh}) are the Coulomb matrix elements associated with electron-electron (hole-hole) interaction and V^{eh} with electron-hole interaction.[2] In the case of monolayer TMDCs, we use the following

[1] This modelling of the microscopic carrier occupations is facilitated by ignoring spatial transport of carriers, as this is more easily represented at the macroscopic level through a diffusion model (cf. Eq 24). The two (microscopic and macroscopic) pictures can still be reconciled, or one can introduce a microscopic transport model as presented in Hess and Kuhn [35].

[2] We are neglecting Auger-like processes due to the high band gap energy.

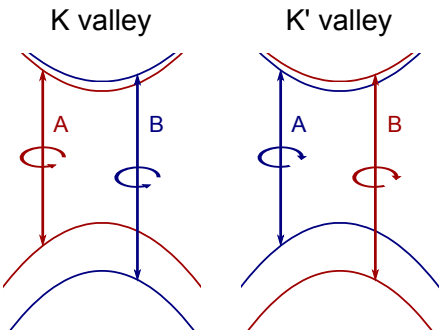

Figure 6: Band structure of a TMDC monolayer close to the K and K' points of the (hexagonal) reciprocal lattice. The colour identify the spin polarisation of the band/exciton, while the arrow shows the allowed optical transitions and their polarisation.

screened version of the two-dimensional Coulomb matrix element

$$V_{\mathbf{q}} = \frac{e^2}{\epsilon_0 \epsilon_s A} \frac{1}{q\,(1 + r_0 q)}\,, \tag{30}$$

which has been extensively discussed in the TMDC literature [38–43]. Here e is the elementary charge, ϵ_0 the dielectric constant and A the area. The screening length is given by $r_0 = t\epsilon_\perp/\epsilon_s$, with the inplane dielectric constant of the bulk material, $\epsilon_\perp$ and the monolayer thickness, t. The dielectric constant ϵ_s accounts for screening from the environment

$$\epsilon_s = \epsilon_{\text{super}} + \epsilon_{\text{sub}}, \tag{31}$$

which is the sum of the dielectric constant of the substrate, ϵ_{sub}, and the superstrate, ϵ_{super}. Indeed, it was found that the exciton binding energy depends sensibly on the surrounding material [44, 45].

Another interesting feature that was observed in TMDC monolayers is that both the valence and conduction band are split by a strong spin-orbit coupling, resulting in the presence of two strong resonances in the absorption spectra, termed A and B excitons. Furthermore their band structure show the presence of two valleys, with the same transition energies, located at the K and K' points of the hexagonal reciprocal lattice, as is sketched in Fig. 6. In order to study the dynamics of this 8 band system, we expand Eq. 28 to include a composite index, $\nu \in \{\text{AK}, \text{BK}, \text{AK}', \text{BK}'\}$, on most quantities, resulting in four sets of Maxwell-Bloch equations, one for each of the electron/hole band pairs. This different sets of equations are further weakly coupled through Coulomb interaction.

Due to the missing inversion symmetry in the monolayer, however, the K and K' valley are not equivalent. This has a double effect: it produces a swap in the ordering of the spin-split bands and it introduces different optical selection rules for the transitions. Indeed it was observed that different valleys couple to circularly polarised light of opposite handedness [46]. This can be included in the model by replacing the dipole matrix elements, $\mathbf{d}_\nu$, with the complex vectors

$$\mathbf{M}^{cv}_\nu = (M_x, \pm \mathrm{i} M_y, 0)\,, \tag{32}$$

where $M_{x/y} \geq 0$, the $\pm$ selects the handedness and x and y are the in-plane directions of the monolayer.

Another consequence of the lack of inversion symmetry is the presence of even harmonics in the optical response of TMDC monolayers, in particular a very strong second harmonic generation has been observed experimentally and has been a major research focus due to its possible applications [47–52]. However, the equations of motion we have presented up to know can only be used to reproduce odd harmonic generation. We therefore introduce in the Hamiltonian that generates Maxwell-Bloch equation and additional term that describes a further coupling with the field

$$\mathcal{H}_{\text{pd}} = -e\mathbf{E}\,(\mathbf{r}, t) \cdot \sum_{\nu,\mathbf{k}} \left[\mathbf{M}^c_\nu \hat{c}^\dagger_{\nu,\mathbf{k}} \hat{c}_{\nu,\mathbf{k}} - \mathbf{M}^v_\nu \hat{d}^\dagger_{\nu,\mathbf{k}} \hat{d}_{\nu,\mathbf{k}}\right] \tag{33}$$

where $\hat{c}^\dagger_{\nu,\mathbf{k}}$ ($\hat{d}^\dagger_{\nu,\mathbf{k}}$) and $\hat{c}_{\nu,\mathbf{k}}$ ($\hat{d}_{\nu,\mathbf{k}}$) are the electron (hole) creation and annihilation operators. This term describes the energy present in the system due to the direct interaction of the optical fields with the

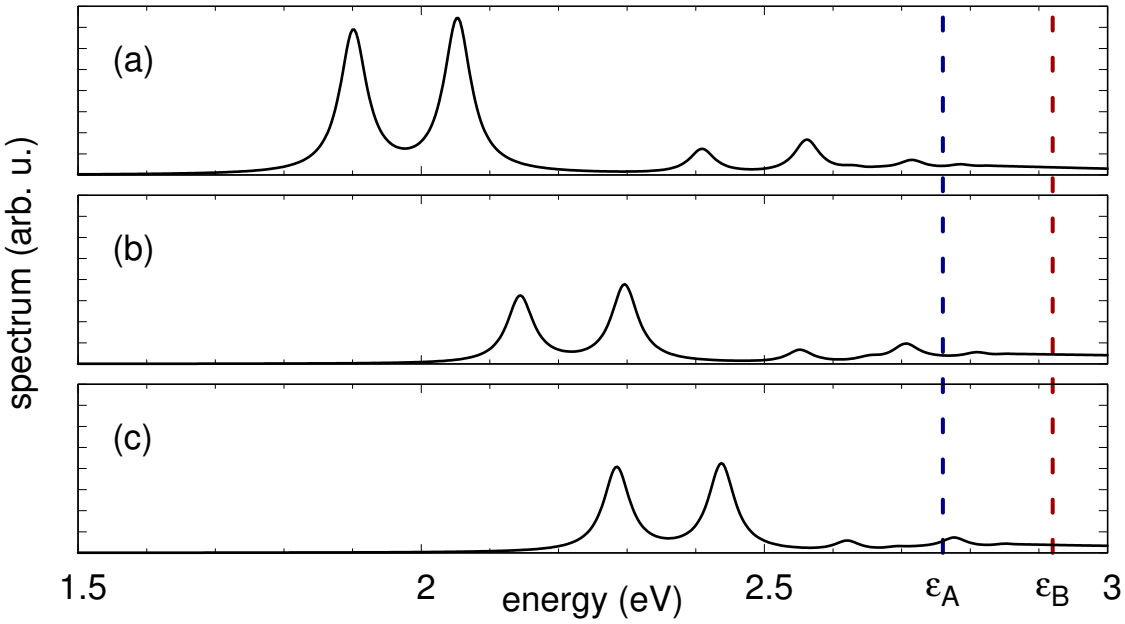

Figure 7: Absorption spectra of MoS_2 in different environments, i.e., for different values of ϵ_s. The vertical dashed lines identify the bandgap energy for the A and B bands. (a) Free-standing. (b) Glass substrate. (c) Glass substrate and superstrate.

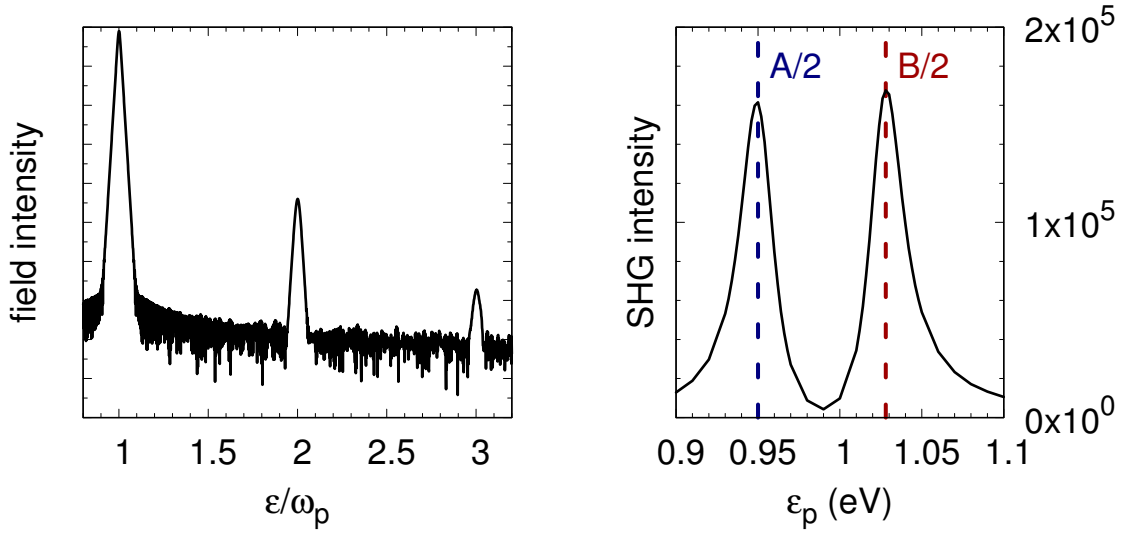

(a) Non linear optical response of a free-standing MoS_2 monolayer excited with a strong laser pulse of central frequency ω_p at half the energy of the A exciton. The peaks at $2\omega_p$ and $3\omega_p$ are, respectively, the second and third harmonic generation. Note that the y axis is logarithmic.

(b) Strength of the SHG (cf. peak height in Fig. 8a) when sweeping the exciting frequency across the region containing the A and B excitons.

electronic states that are polarised due to the broken inversion symmetry. In particular, we choose the intraband dipole moment of the conduction (valence) band to be laying in the monolayer plane

$$\mathbf{M}_{\nu}^{c(v)} = \left(M_{\nu,x}^{c(v)}, M_{\nu,y}^{c(v)}, 0\right). \tag{34}$$

A similar Hamiltonian, including permanent intraband dipoles and a second order susceptibility $\chi^{(2)}$, has been used to describe tilted quantum wells [53, 54]. Furthermore, we note that the SHG is polarization dependent, i.e. for certain symmetry axes the second harmonic is weak [52, 55] and for not perfectly aligned stacked TMDC layers strong second harmonic signals can be found [56, 57]. To account for such effects a **k**-dependent matrix element could be taken into account, while here we make the approximation of **k**-independent intraband dipole moment.

In the equations of motions (cf. Eq. (28)) the interaction with the intraband dipole enters in the polarization $\mathcal{P}_{\nu,\mathbf{k}}(\mathbf{r},t)$ via

$$\partial_t \mathcal{P}_{\nu,\mathbf{k}}(\mathbf{r},t)|_{\mathcal{H}_{pd}} = -\frac{\mathrm{i}}{\hbar}\mathbf{E}(\mathbf{r},t)\cdot\left(\mathbf{M}_{\nu}^{c}-\mathbf{M}_{\nu}^{v}\right)\mathcal{P}_{\nu,\mathbf{k}}(\mathbf{r},t) \tag{35}$$

The equations of motion now also contain a coupling in second order of the electric field in the polarization, hence we can calculate second harmonic generation and also higher even harmonics. We stress that here we have a dynamical electric field $\mathbf{E}(\mathbf{r},t)$ and obtain the non-linear signals directly from the dynamical calculation.

Lastly, we change the macroscopic polarisation (cf. Eq. 13) that acts as a source in Maxwell's equation in order to allow the changes in the model to affect the fields

$$\mathbf{P}(\mathbf{r},t) = \frac{N_{\mathrm{QW}}}{L_{\mathrm{act}}}\frac{e}{A}\sum_{\nu,\mathbf{k}}\left(\mathcal{P}_{\nu,\mathbf{k}}^{*}(\mathbf{r},t)\,\mathbf{M}_{\nu}^{cv}+\mathcal{P}_{\nu,\mathbf{k}}(\mathbf{r},t)\,\mathbf{M}_{\nu}^{cv*}\right) \tag{36}$$

The results shown in the following sections are obtained for a MoS_2 monolayer, using the parameters summarised in Tab. 1.

effective mass electron	m^e	0.480 m_0
effective mass hole A	m_A^v	0.575 m_0
effective mass hole B	m_B^v	0.660 m_0
band gap	E_{gap}	2.84 eV
valence band splitting	Δ_v	160 meV
conduction band splitting	Δ_c	0 meV
dipole matrix element	$\lvert M^{cv}\rvert_x = \lvert M^{cv}\rvert_y$	0.2 nm
intraband dipole	$\lvert M^c - M^v\rvert_{x,y}$	0.02 nm
layer thickness	d	0.312 nm
in-plane dielectric constant	$\varepsilon_\perp$	12
dephasing rate	γ	1/30 fs^{-1}

Table 1: Parameters of MoS_2 with m_0 being the free electron mass

4.2 Linear response

We start by analysing the optical response of the monolayer in linear regime as this allows us to validate some of the features of our model. To do so, we send a weak pulse from one side onto the structure, e.g. a free-standing TMDC monolayer or a more sophisticated photonic structure with an embedded TMDC monolayer. The light pulse then propagates through the structure and interacts with the TMDC monolayer. We record the reflected and transmitted fields with the intensities I_{refl} and I_{trans}, respectively [34]. The spectrum α is then calculated via

$$\alpha(\omega) = 1 - \frac{I_{refl}(\omega) + I_{trans}(\omega)}{I_{inc}(\omega)} \tag{37}$$

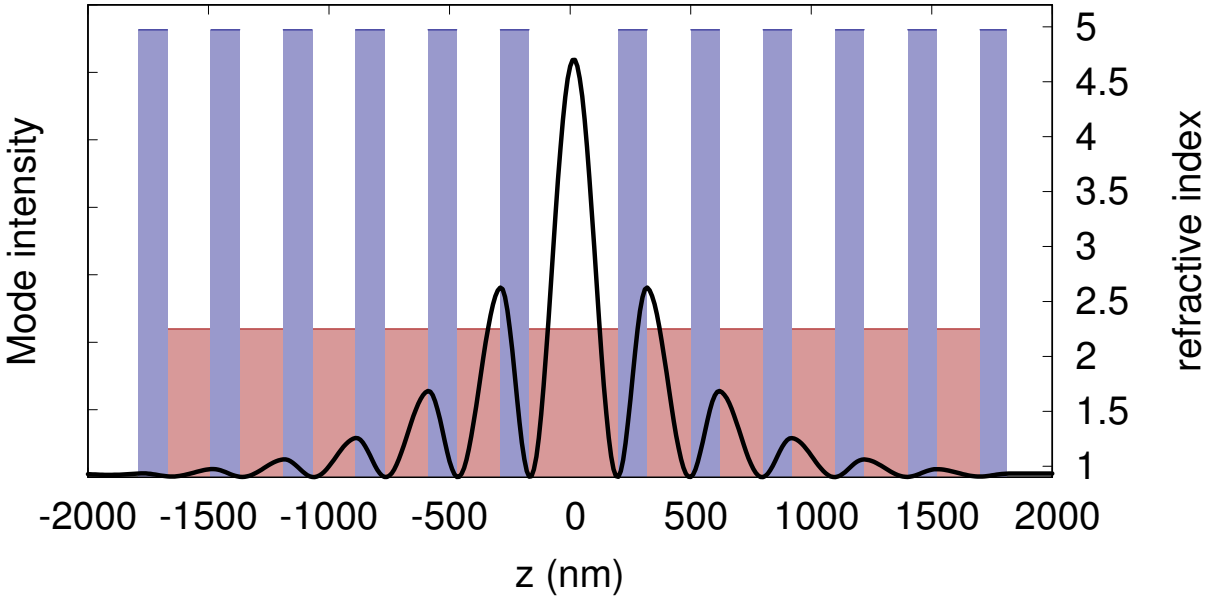

Figure 9: (colour) Refractive index profile of the dielectric cavity used to enhance SHG in MoS_2 monolayers. (black) Profile of the fundamental optical mode of the cavity.

with I_{inc} the intensity of the incoming pulse. We choose the polarization of the incoming pulse to be right-handed circular polarization, thereby addressing only the K-valley. The results are the same for left-handed circular polarization, where only the K' excitons would appear.

First we characterise the linear response of a free-standing monolayer whose absorption spectrum is shown in Fig. 7a. This absorption shows two strong resonances at 1.90 eV and 2.05 eV. We attribute these to the formation of ground state excitons in the A and B band that are known to appear when including Coulomb interaction in dynamical model[34]. From these resonances and the bandgap values reported in Table 1 we can calculate the binding energy of the excitons, which turns out to be of about 850 meV. This is comparable with the strong binding energies reported in previous theoretical and experimental works [58, 40, 59–61, 41]. Furthermore, the energy splitting between the A and B exciton is dominated by the spin orbit splitting of the bands (cf. Table 1), whereas the different strength can be traced back to the different band gap energies.

Due to the strong Coulomb interaction and strong binding energy, our absorption spectrum also shows resonances corresponding to the first few excited states of the A and B excitons. Studies of the exciton series in TMDC monolayers is still a very active research field, because strong deviations from the Rydberg series were found [47, 59].

Another interesting aspect that has been observed in previous work is the strong dependence of TMDCs exciton energies on the dielectric environment. This is a consequence of the material being a monolayer resulting in Coulomb field lines that can penetrate deep into the sub- and superstrate [38–41]. We show how this effect changes the absorption spectrum of a MoS_2 monolayer in Fig. 7b, where we include in the simulation a glass substrate with a refractive index $n = 1.50$. This results in a blue-shift of the A and B exciton peaks by about 250 meV to energies of 2.15 eV and 2.30 eV respectively. Another effect on the energy of the exciton might be the renormalization of the band gap, as reported from DFT calculations [62, 63, 45], which can be easily included by changing the input parameters of the simulation.

Lastly we consider the case of a MoS_2 monolayer sandwiched in glass. This is of particular importance when the monolayer is going to be embedded in a dielectric cavity. In Fig. 7c we see a further decrease in exciton binding energies resulting in excitonic resonances at 2.28 eV and 2.43 eV.

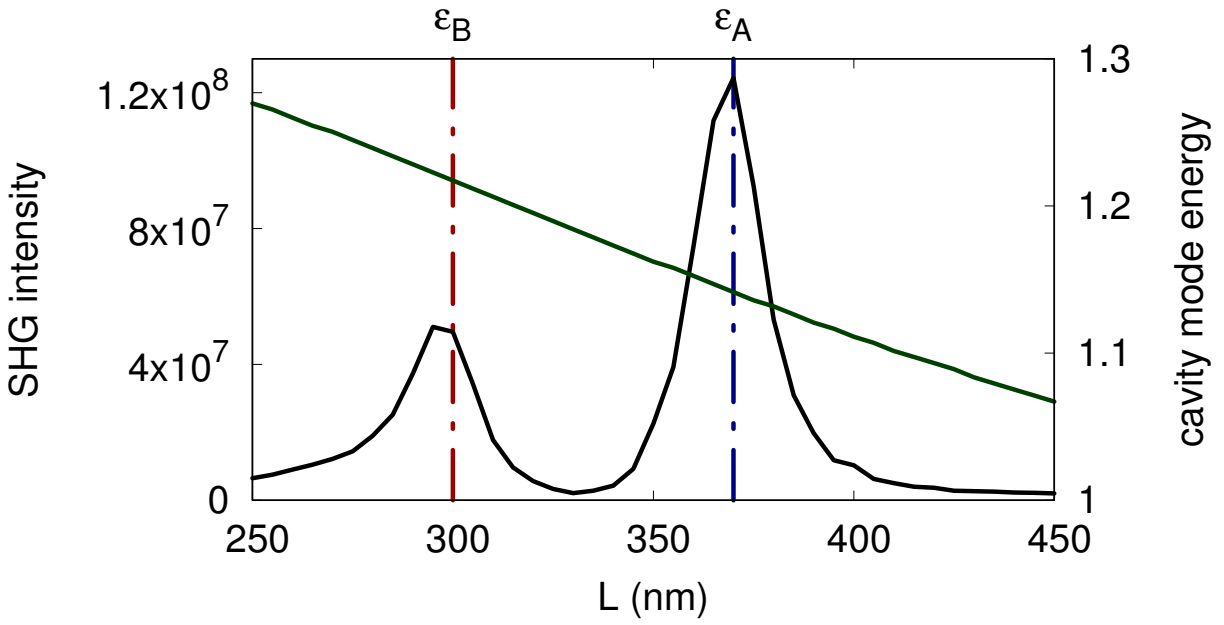

Figure 10: (green,right axis) Dependence of the energy of the fundamental mode over the length of the cavity. (black, left axis) Intensity of SHG generated by the TMDC monolater when excited resonant with the energy of the optical mode of the cavity.

4.3 Non-linear response

As a first example we consider the non-linear optical response of a freestanding MoS_2 monolayer. For the optical excitation we use a sech pulse of the form $E(t) = E_0 \cos(\omega_p t)\mathrm{sech}(t/\tau)$ with linear polarization. The laser pulse excites the system at the energy $\varepsilon_p = \hbar\omega_p$ with a full width at half maximum FWHM of the pulse $2\tau \log(2+\sqrt{3}) = 200$ fs. The strength of the pulse is set to $E_0 = 10^8$ V/m. We first set the energy of the laser pulse to half of the A-exciton energy with $\varepsilon_p = 0.95$ eV and calculate the spectrum shown in Fig. 8a. Note that the spectrum is shown on a logarithmic scale.

In the spectrum the most pronounced peak occurs at the exciting frequency $\epsilon = \hbar\omega_p = 0.95$ eV being half of the A exciton energy. At multiples of the exciting frequency we see additional peaks appearing, because higher harmonics generation takes place. The peak at $\epsilon = 2\hbar\omega_p$ is the second harmonic generation (SHG) signal and coincides with the energy of the A exciton of a freestanding monolayer. The field of the second harmonic is about 8 orders of magnitude below the intensity of the fundamental peak. We also see the appearance of the third harmonic at $\epsilon = 3\hbar\omega_p$. Here, the field is about 13 orders of magnitude lower than the fundamental reflecting the higher order of the process. Third harmonic generation has also been experimentally observed in TMDC monolayers [57]. We emphasize, that we calculate the higher harmonic generation within a full dynamical picture without the explicit use of the susceptibility. In our approach, the interaction of the light field with the Coulomb-interacting carriers in the semiconductor leads to the generation of these non-linear optical signals.

It is also interesting to note that even though the exciton energies are not an explicit input in our calculation, but are rather a result of our model, we find a strong dependence of the strength of the higher harmonic generation on the exciton energy. For this, we sweep the energy of the exciting laser pulse ε_p and plot the resulting strength of the second harmonic signal in Fig. 8b. We find that at $\varepsilon_p = 0.95$ eV and $\varepsilon_p = 1.03$ eV the second harmonic generation is particularly strong. These energies can be identified with half of the energy of the A and B exciton of the freestanding monolayer, respectively. We conclude, that non-linear processes are much more efficient when a final state for the higher harmonic is present.

To enhance the non-linear optical response of the TMDC monolayer, we propose to embed the TMDC into a photonic structure consisting of two distributed Bragg mirrors of layers of glass (refractive index 1.50) and silicon nitrite (refractive index 2.23) as shown in Fig. 9. Each glass layer is

chosen as 180 nm thick and each silicon nitride layer is 120 nm thick. This results in a broad photonic stop band around an energy of 1 eV, with a sharp resonance (corresponding to a cavity mode) whose energy can be tuned by changing the length of the cavity. This dependence is illustrated in Fig. 10 and appears to be approximately linear as in this region the modes lie well within the photonic stop band. The fundamental mode of the cavity for a length of $L = 370$ nm is represented by the black line in Fig. 9 and shows that a strong field enhancement can be achieved.

Now we include the TMDC monolayer at the field maximum of the cavity and consider the strength of the second harmonic signal. Note that the exciting frequency of the impinging laser pulse is always chosen such that it matches the frequency of the cavity mode. The strength of the second harmonic generation as function of cavity length is displayed in Fig. 10 (black curve). We find that for a cavity length of 300 nm and for 370 nm a pronounced enhancement occurs as for this length the energy of the cavity mode becomes resonant with half of the energy of the B and A excitons respectively. Due to the cavity structure the second harmonic signal is up to 3 orders of magnitude stronger than for the free standing monolayer. We have thus managed to considerably enhance the nonlinearity of the semiconductor monolayer.

5 Research plan

During the final year of the project there are a number of exciting avenues that have been started.

Thanks to recent experimental results [64] we can see that a Fabry-Pérot QW laser should have an multimode behaviour, in which multiple longitudinal modes in competition with each other are simultaneously emitting. By comparing this with our simulation, we are now investigating the possibility that a previously well-accepted diffusion model is not suitable for the description of carrier transport in our case of a multi-mode laser, as experimentally measured values of $D \simeq 1 \times 10^{-3}$ m$^2/s$[35, 65, 66] reduce our simulation to single-mode behaviour. Our current understanding is that this is a consequence of our innovative high (sub-wavelength) spatial resolution, whereas the classical diffusion equation was derived in the context of the slowly varying envelope approximation.

In order to exclude a dependence of this behaviour on system size, we are now working on extending the length of the semiconductor, as well as the simulation time. Even though we will never be able to achieve a size comparable with a realistic experimental setup, we hope to be able to identify a trend in the value of D for which the change from multimode to singlemode behaviour happens (Cf. Fig. 5b).

In Sec. 4 we showed how our model of combined semiconductor and field dynamics can be readily extended to describe different systems as well as different optical environments. Thanks to FDTD, our simulation can easily be extended to metallic or metallodielectric cavities in order to exploit plasmonic effects to further enhance and confine the field [37].

References

[1] V M Axt and S Mukamel. Nonlinear optics of semiconductor and molecular nanostructures; a common perspective. *Rev. Mod. Phys.*, 70(1):145, Jan 1998.

[2] D Yelin and Y Silberberg. Laser scanning third-harmonic-generation microscopy in biology. *Opt. Express*, 5(8):169, 1999.

[3] B Weigelin, G-J Bakker, and P Friedl. Third harmonic generation microscopy of cells and tissue organization. *J. Cell Sci.*, 129(2):245, 2016.

[4] Y-C Chen, S-Y Lee, Y Wu, K Brink, D-B Shieh, T D Huang, R R Reisz, and C-K Sun. Third-harmonic generation microscopy reveals dental anatomy in ancient fossils. *Opt. Lett.*, 40(7):1354, 2015.

[5] C Sirtori, F Capasso, D L Sivco, and A Y Cho. Giant, triply resonant, third-order nonlinear susceptibility χ 3 ω (3) in coupled quantum wells. *Phys. Rev. Lett.*, 68(7):1010, 1992.

[6] J N Heyman, K Craig, B Galdrikian, M S Sherwin, K Campman, P F Hopkins, S Fafard, and A C Gossard. Resonant harmonic generation and dynamic screening in a double quantum well. *Phys. Rev. Lett.*, 72(14):2183, 1994.

[7] T S Mosely, A Belyanin, C Gmachl, D L Sivco, M L Peabody, and Alfred Y Cho. Third harmonic generation in a quantum cascade laser with monolithically integrated resonant optical nonlinearity. *Opt. Express*, 12(13):2972, 2004.

[8] S Sauvage, P Boucaud, F Glotin, R Prazeres, J-M Ortega, A Lemaitre, J-M Gérard, and V Thierry-Mieg. Third-harmonic generation in inas/gaas self-assembled quantum dots. *Phys. Rev. B*, 59(15):9830, 1999.

[9] G Wang. Third-harmonic generation in cylindrical parabolic quantum wires with an applied electric field. *Phys. Rev. B*, 72(15):155329, 2005.

[10] S-Y Hong, J I Dadap, N Petrone, P-C Yeh, J Hone, and R M Osgood Jr. Optical third-harmonic generation in graphene. *Phys. Rev. X*, 3(2):021014, 2013.

[11] R Wang, H-C Chien, J Kumar, N Kumar, H-Y Chiu, and H Zhao. Third-harmonic generation in ultrathin films of MoS2. *ACS Appl. Mater. Interfaces*, 6(1):314, 2013.

[12] R W Ziolkowski, J M Arnold, and D M Gogny. Ultrafast pulse interactions with two-level atoms. *Phys. Rev. A*, 52(4):3082, 1995.

[13] A Pusch, J M Hamm, and O Hess. Controllable interaction of counterpropagating solitons in three-level media. *Phys. Rev. A*, 82(2):023805, 2010.

[14] A Pusch, J M Hamm, and O Hess. Femtosecond nanometer-sized optical solitons. *Phys. Rev. A*, 84(2):023827, 2011.

[15] S Wuestner, A Pusch, K L Tsakmakidis, J M Hamm, and O Hess. Overcoming losses with gain in a negative refractive index metamaterial. *Phys. Rev. Lett.*, 105(12):127401, 2010.

[16] A Fang, T Koschny, and C M Soukoulis. Self-consistent calculations of loss-compensated fishnet metamaterials. *Phys. Rev. B*, 82(12):121102, 2010.

[17] S Wuestner, A Pusch, K L Tsakmakidis, J M Hamm, and O Hess. Gain and plasmon dynamics in active negative-index metamaterials. *Phil. Trans. R. Soc. A*, 369(1950):3525, 2011.

[18] S Wuestner, J M Hamm, A Pusch, F Renn, K L Tsakmakidis, and O Hess. Control and dynamic competition of bright and dark lasing states in active nanoplasmonic metamaterials. *Phys. Rev. B*, 85(20):201406, 2012.

[19] T Pickering, J M Hamm, A F Page, S Wuestner, and O Hess. Cavity-free plasmonic nanolasing enabled by dispersionless stopped light. *Nat Comms*, 5:4972, Sep 2014.

[20] S T Cundiff, A Knorr, J Feldmann, S W Koch, E O Göbel, and H Nickel. Rabi flopping in semiconductors. *Phys. Rev. Lett.*, 73(8):1178, 1994.

[21] A Schülzgen, R Binder, M E Donovan, M Lindberg, K Wundke, H M Gibbs, G Khitrova, and N Peyghambarian. Direct observation of excitonic rabi oscillations in semiconductors. *Phys. Rev. Lett.*, 82(11):2346, 1999.

[22] F Rossi and T Kuhn. Theory of ultrafast phenomena in photoexcited semiconductors. *Rev. Mod. Phys.*, 74(3):895, 2002.

[23] H Haug and S W Koch. *Quantum theory of the optical and electronic properties of semiconductors*, volume 5. World Scientific, 2004.

[24] D Reiter, M Glanemann, V M Axt, and T Kuhn. Controlling the capture dynamics of traveling wave packets into a quantum dot. *Phys. Rev. B*, 73(12):125334, 2006.

[25] D Reiter, M Glanemann, V M Axt, and T Kuhn. Spatiotemporal dynamics in optically excited quantum wire-dot systems: Capture, escape, and wave-front dynamics. *Phys. Rev. B*, 75(20): 205327, 2007.

[26] R Rosati and F Rossi. Microscopic modeling of scattering quantum non-locality in semiconductor nanostructures. *Appl. Phys. Lett.*, 103(11):113105, 2013.

[27] Q T Vu, H Haug, O D Mücke, T Tritschler, M Wegener, G Khitrova, and H M Gibbs. Light-induced gaps in semiconductor band-to-band transitions. *Phys. Rev. Lett.*, 92(21):217403, May 2004.

[28] O D Mücke, T Tritschler, M Wegener, U Morgner, and F X Kärtner. Signatures of carrier-wave rabi flopping in GaAs. *Phys. Rev. Lett.*, 87(5):057401, Jul 2001.

[29] A M Nemilentsau, G Ya Slepyan, A A Khrutchinskii, and S A Maksimenko. Third-order optical nonlinearity in single-wall carbon nanotubes. *Carbon*, 44(11):2246, Sep 2006.

[30] C Stanciu, R Ehlich, V Petrov, O Steinkellner, J Herrmann, I V Hertel, G Ya Slepyan, A A Khrutchinski, S A Maksimenko, F Rotermund, Campbell E E B, and Rohmund F. Experimental and theoretical study of third-order harmonic generation in carbon nanotubes. *App. Phys. Lett.*, 81(21):4064, 2002.

[31] K Böhringer and O Hess. A full-time-domain approach to spatio-temporal dynamics of semiconductor lasers. i. theoretical formulation. *Prog. Quant. Electron.*, 32:159, 2008.

[32] K Böhringer and O Hess. A full time-domain approach to spatio-temporal dynamics of semiconductor lasers. ii. spatio-temporal dynamics. *Prog. Quant. Electron.*, 32(5):247, 2008.

[33] R Buschlinger, M Lorke, and U Peschel. Light-matter interaction and lasing in semiconductor nanowires: A combined finite-difference time-domain and semiconductor bloch equation approach. *Phys. Rev. B*, 91(4):045203, 2015.

[34] Stefano Guazzotti, Andreas Pusch, Doris E Reiter, and Ortwin Hess. Dynamical calculation of third-harmonic generation in a semiconductor quantum well. *Phys. Rev. B*, 94(11):115303, 2016.

[35] Ortwin Hess and Tilmann Kuhn. Spatio-temporal dynamics of semiconductor lasers: Theory, modelling and analysis. *Progress in Quantum Electronics*, 20(2):85–179, 1996.

[36] Klaus Böhringer and Ortwin Hess. A full-time-domain approach to spatio-temporal dynamics of semiconductor lasers. I. Theoretical formulation. *Progress in Quantum Electronics*, 32(5-6): 159–246, 2008.

[37] Chris Oubre and Peter Nordlander. Optical properties of metallodielectric nanostructures calculated using the finite difference time domain method. *The Journal of Physical Chemistry B*, 108 (46):17740–17747, 2004.

[38] L. V. Keldysh. Coulomb interaction in thin semiconductor and semimetal films, 1979.

[39] Pierluigi Cudazzo, Ilya V. Tokatly, and Angel Rubio. Dielectric screening in two-dimensional insulators: Implications for excitonic and impurity states in graphane. *Physical Review B*, 84(8): 085406, 2011.

[40] T. C. Berkelbach, M. S. Hybertsen, and D. R. Reichman. Theory of neutral and charged excitons in monolayer transition metal dichalcogenides. *Phys. Rev.* B, 88:045318, 2013.

[41] Alexey Chernikov, Timothy C. Berkelbach, Heather M. Hill, Albert Rigosi, Yilei Li, Ozgur Burak Aslan, David R. Reichman, Mark S. Hybertsen, and Tony F. Heinz. Exciton Binding Energy and Nonhydrogenic Rydberg Series in Monolayer WS_2. *Physical Review Letters*, 113(7):076802, 2014.

[42] S. Latini, T. Olsen, and K. S. Thygesen. Excitons in van der Waals heterostructures: The important role of dielectric screening. *Physical Review B*, 92(24):245123, dec 2015.

[43] Diana Y. Qiu, Felipe H. da Jornada, and Steven G. Louie. Screening and many-body effects in two-dimensional crystals: Monolayer MoS_2. *Physical Review B*, 93(23):235435, jun 2016.

[44] A. Chernikov, T. C. Berkelbach, H. M. Hill, A. Rigosi, Y. Li, O. B. Aslan, D. R. Reichman, M. S. Hybertsen, and T. F. Heinz. Exciton binding energy and nonhydrogenic Rydberg series in monolayer WS_2. *Phys. Rev. Lett.*, 113:076802, 2014.

[45] Y. Lin, X. Ling, L. Yu, S. Huang, A. L. Hsu, Y.-H. Lee, J. Kong, M. S. Dresselhaus, and T. Palacios. Dielectric screening of excitons and trions in single-layer MoS_2. *Nano lett.*, 14:5569, 2014.

[46] G. Berghäuser and E. Malic. Analytical approach to excitonic properties of MoS_2. *Phys. Rev.* B, 89:125309, 2014.

[47] G. Wang, X. Marie, I. Gerber, T. Amand, D. Lagarde, L. Bouet, M. Vidal, A. Balocchi, and B. Urbaszek. Giant enhancement of the optical second-harmonic emission of WSe_2 monolayers by laser excitation at exciton resonances. *Phys. Rev. Lett.*, 114:097403, 2015.

[48] L. M. Malard, T. V. Alencar, A. P. M. Barboza, K. F. Mak, and A. M. de Paula. Observation of intense second harmonic generation from MoS_2 atomic crystals. *Phys. Rev.* B, 87:201401(R), 2013.

[49] N. Kumar, S. Najmaei, Q. Cui, F. Ceballos, P. M. Ajayan, J. Lou, and H. Zhao. Second harmonic microscopy of monolayer MoS_2. *Phys. Rev.* B, 87:161403, 2013.

[50] H. Zeng, G.-B. Liu, J. Dai, Y. Yan, B. Zhu, R. He, L. Xie, S. Xu, X. Chen, W. Yao, and X. Cui. Optical signature of symmetry variations and spin-valley coupling in atomically thin tungsten dichalcogenides. *Sci. Rep.*, 3:1608, 2013.

[51] C. Janisch, Y. Wang, D. Ma, N. Mehta, A. L. Elías, N. Perea-López, M. Terrones, V. Crespi, and Z. Liu. Extraordinary second harmonic generation in tungsten disulfide monolayers. *Sci. Rep.*, 4:5530, 2014.

[52] K. L. Seyler, J. R. Schaibley, P. Gong, P. Rivera, A. M. Jones, S. Wu, J. Yan, D. G. Mandrus, W. Yao, and X. Xu. i Electrical control of second-harmonic generation in a WSe_2 monolayer transistor. *Nat. Nanotechnol.*, 10:407–, 2015.

[53] L. Tsang, D. Ahn, and S. L. Chuang. Electric field control of optical second-harmonic generation in a quantum well. *Appl. Phys. Lett.*, 52:697, 1988.

[54] E. Rosencher, A Fiore, B Vinter, V Berger, Ph Bois, and J Nagle. Quantum Engineering of Optical Nonlinearities. *Science*, 271(5246):168–173, jan 1996.

[55] Y. Li, Y. Rao, K. F. Mak, Y. You, S. Wang, C. R. Dean, and T. F. Heinz. Probing symmetry properties of few-layer MoS_2 and h-BN by optical second-harmonic generation. *Nano lett.*, 13: 3329, 2013.

[56] W.-T. Hsu, Z.-A. Zhao, L.-J. Li, C.-H. Chen, M.-H. Chiu, P.-S. Chang, Y.-C. Chou, and W.-H. Chang. Second harmonic generation from artificially stacked transition metal dichalcogenide twisted bilayers. *ACS nano*, 8:2951, 2014.

[57] J. Zhang, M. Ye, S. Bhandari, A. K. M. Muqri, F. Long, S. Bigham, Y. K. Yap, and J. Y. Suh. Enhanced second and third harmonic generations of vertical and planar spiral MoS_2 nanosheets. *Nanotech.*, 28(295301):295301, 2017.

[58] D. Y. Qiu, F. H. da Jornada, and S. G. Louie. Optical Spectrum of MoS_2 : Many-Body Effects and Diversity of Exciton States. *Phys. Rev. Lett.*, 111:216805, 2013.

[59] B. Scharf, T. Frank, M. Gmitra, J. Fabian, I. Žutić, and V. Perebeinos. Excitonic Stark effect in MoS_2 monolayers. *Phys. Rev.* B, 94:245434, 2016.

[60] F. Wu, F. Qu, and A. H. Macdonald. Exciton band structure of monolayer MoS_2. *Phys. Rev.* B, 91:075310, 2015.

[61] Bairen Zhu, Xi Chen, and Xiaodong Cui. Exciton binding energy of monolayer WSâ. *Scientific reports*, 5:9218, 2015.

[62] H.-P. Komsa and A. V. Krasheninnikov. Effects of confinement and environment on the electronic structure and exciton binding energy of MoS_2 from first principles. *Phys. Rev.* B, 86:241201, 2012.

[63] M. M. Ugeda, A. J. Bradley, S.-F. Shi, F. H. da Jornada, Y. Zhang, D. Y. Qiu, W. Ruan, S.-K. Mo, Z. Hussain, Z.-X. Shen, F. Wang, S. G. Louie, and M. F. Crommie. Giant bandgap renormalization and excitonic effects in a monolayer transition metal dichalcogenide semiconductor. *Nat. Mat.*, 13:1091, 2014.

[64] H Cao and S Bittner. Personal communication, 2017.

[65] Ortwin Hess. Spatio-temporal complexity in multi-stripe and broad-area semiconductor lasers. *Chaos, Solitons & Fractals*, 4(8-9):1597–1618, 1994.

[66] John R Marciante and Govind P Agrawal. Spatio-temporal characteristics of filamentation in broad-area semiconductor lasers. *IEEE Journal of Quantum Electronics*, 33(7):1174–1179, 1997.